Journal of Materials Chemistry A

ROYAL SOCIETY OF CHEMISTRY

PAPER

View Article Online
View Journal | View Issue

Cite this: J. Mater. Chem. A, 2024, 12, 12533

Atomically dispersed Ru sites on MOF-derived NC-ZnO for efficient oxygen evolution reaction in acid media†

Sagar Varangane,[ac] Ragunath Madhu,[cd] Saad Mehmood,[ac] Bhavya Jaksani,[ac] Vidha Bhasin,[g] B. Moses Abraham,[f] Ammavasi Nagaraj,[e] Chandra Shobha Vennapoosa,[ac] B. V. Subba Reddy,[ab] Subrata Kundu *[cd] and Ujjwal Pal *[ac]

Developing acid-stable oxygen evolution/reduction reaction (OER/ORR) electrocatalysts is essential for high-performance water splitting. Still, the slow kinetics of the ORR and OER during the discharge and charge processes seriously impede their advancement in these performances. This report outlines the creation of a nitrogen-doped porous carbon matrix (NC) produced from a zeolitic imidazolate framework (ZIF-8). The matrix includes spatially engineered ultra-low loaded Ru atomic sites and is examined in the context of electrocatalytic oxygen evolution studies. The systematic analysis and computational studies reveal that the Ru atomic sites act as central driving forces, and their formation is confirmed through X-ray photoelectron spectroscopy (XPS) and X-ray absorption spectroscopy (XAS) analyses, specifically X-ray absorption near-edge structure (XANES) and extended X-ray absorption fine structure (EXAFS). These analyses emphasize the presence of Ru–O bonds at approximately 1.4 Å. Moreover, these results were validated by HRTEM, STEM, and HAADF investigations which emphasize the dispersion of atom-scale Ru on the NC(ZnO). $Ru_{1.75}$@NC(ZnO) shows a low overpotential (320 mV) at a current density of 10 mA cm^{-2} for the OER because of the high active site utilization. Importantly, the $Ru_{1.75}$@NC(ZnO) electrode displays an admirable specific capacitance value of 0.0501 mF cm^{-2} with notable durability of the capacitor after 500 cycles. The studies revealed that the introduction of monometallic Ru into ZIF-derived ZnO tunes intermediate adsorption energies and promotes the reactions by demanding lesser free energy in the water dissociation process. This research advances the pursuit of creating high-efficiency electrocatalysts with single-site structures, aiming for maximum atomic utilization efficiency in oxygen evolution reactions (OERs), particularly on templates derived from ZIFs.

Received 25th January 2024
Accepted 16th April 2024

DOI: 10.1039/d4ta00586d

rsc.li/materials-a

Introduction

Electrocatalysts thrive tremendously in renewable energy conversion and storage because they control electrochemical processes' selectivity, efficiency, and rate.[1] These catalysts have been used in various transformations such as CO oxidation,[2,3] hydrogenation,[4,5] dehydrogenation,[6] ORR,[7] (HER)[8] OER,[9,10] and other electrocatalytic reactions.[11–13] Researchers have spent decades developing potent OER electrocatalysts to improve kinetics,[14,15] particularly in acidic media, facilitating high mass-transfer speed and product purity.[16] Robust and efficient electro-catalysts are required to expedite reaction kinetics.[17–19] A four-electron transfer process produces oxygen gas from water in the OER. The OER process comprises two stages: O–H bond cleavage and O–O bond formation, which is a four-electron–proton coupled reaction. The commonly acknowledged overall reaction pathways for the OER are: $4OH^- \rightarrow O_2 + 2H_2O + 4e^-$ (alkaline

[a]Department of Energy & Environmental Engineering, CSIR-Indian Institute of Chemical Technology, Hyderabad-500007, India. E-mail: upal03@gmail.com; ujjwalpal@iict.res.in

[b]Centre for Semiochemicals, CSIR- Indian Institute of Chemical Technology, Hyderabad, 500 007, India

[c]Academy of Scientific and Innovative Research (AcSIR), Ghaziabad-201002, India. E-mail: kundu.subrata@gmail.com; skundu@cecri.res.in

[d]Electrochemical Process Engineering (EPE), CSIR-Central Electrochemical Research Institute (CECRI), Karaikudi-630003, Tamil Nadu, India

[e]Department of Chemical Engineering, Indian Institute of Technology Kanpur, Kanpur 208016, India

[f]Departament de Ciència de Material i Química Física & Institut de Química Teòrica i Computacional (IQTCUB), Universitat de Barcelona, c/ Martí i Franquès 1-11, 08028 Barcelona, Spain

[g]Atomic and Molecular Physics Division, Bhabha Atomic Research Centre, Mumbai 400085, India

† Electronic supplementary information (ESI) available. See DOI: https://doi.org/10.1039/d4ta00586d

media); $2H_2O \rightarrow O_2 + 4H^+ + 4e^-$ (acidic media).[20,21] This means that during the reaction, four electrons undergo a transfer from the anode to the cathode, resulting in the generation of oxygen gas. Noble metal electrocatalysts like RuO_2 and IrO_2 were extensively employed for constructing active OER catalysts.[22–24] Still, these catalysts had drawbacks such as substantial expenses and inadequate stability. As a result, it is critical to investigate low-cost and high-efficiency OER electrocatalysts and develop a viable catalyst design strategy. The most common noble metal-based electrocatalysts for the OER are based on Ru and Ir. Although Ir based catalysts exhibit great stability, Cl^- and other anions can quickly poison them. Compared to the IrO_2 catalyst, RuO_2 catalyst is less expensive and shows superior intrinsic performance.[25] Furthermore, Ru-based catalysts exhibit an extensive spectrum of redox state modulation, distinct reaction routes, and an adequate oxidation intermediate binding potential; thus, their OER mass efficiency surpasses that of Ir and other noble metal based catalysts.[26] The developed oxygen electrocatalysts should have both the OER and ORR catalyzing ability to increase voltage yield and reduce the overpotential.[27–29]

A compelling tactic to optimize metal atom utilization and reduce expenses without sacrificing catalytic activity is to downsize noble metals to the atomic level and create single atom catalysts (SACs). In this background metal organic frameworks are emerging as potential electrocatalysts due to their high surface area and tuneable pore structure. The OER performances of M–N–C are observed to be improved when such materials are co-doped with different transition metals.[30] Such carbon-based supporting materials are synthesized by the pyrolysis of nitrogen containing substrates. Zeolitic imidazolate framework-8 (ZIF-8), a unique subclass of crystalline metal organic frameworks (MOFs), has garnered much attention due to its exceptional open crystalline structure, morphological feature with well-defined pores, structural flexibility, tuneable functionality, and high surface area, and has shown exceptional performance for electrocatalytic processes.[31,32] ZIF-8 consists of Zn^{+2} coordinated with nitrogen containing 2-methylimidazole ligand and is a promising material to form N–C substrates.[33,34] One important tactic to increase the electrocatalysts' electrocatalytic activity is to carefully modify their chemical compositions. By using such templates for the decoration of SACs, various noble metals are found to be serving as vital sites for electrocatalytic applications.[35,36] When employing single-atom catalysts (SACs), this is particularly significant since the active metal's size is reduced to nanoclusters or single atoms, which results in nearly full accessibility of the active sites, better atomic utilisation, and exceptional electrical characteristics. The atomic scale synthesis of catalysts can be designed to increase the metal atom-utilization efficacy, thereby reducing the quantity of metal resources used, lowering catalyst costs, and achieving an atom-economic and environmentally friendly combination process. Significant charge transfer or strong interaction between single metal and coordination species of robust supports is necessary to preserve the atomic distribution of single metal atoms in contrast to aggregates in the form of nanoparticles. As a result, single metal atoms of SACs have a distinct electronic structure and transport certain charges that set them above typical metal nanoparticles.[37] Ru is the least expensive platinum group metal and seems to be the best option in terms of cost and activity.[38]

The presence of transition metals in these electrocatalysts facilitates catalytic graphitization during construction at high temperatures, which significantly enhances the carbon matrix's electrical conductivity and crystallinity. In electrochemical processes this modification was found to shield the metals from aggregation and corrosion. Strong Ru–N bonds can be formed to embed single-atomic Ru within an acid-resistant N–C coordination environment, which may enhance Ru's stability and give it high activity.[39] This nitrogen rich proximity of ZIF-8 greatly enhances the performance of ORR or OER catalysts because the lone-pair electron of nitrogen triggers π electrons of the carbon atom, resulting in charge delocalization of the carbon atoms.[40] These structural features bestow single atom catalysts (SACs) with improved catalytic performances and even unique catalytic properties compared with their nanoparticle counterparts. Zuo *et al.* designed a hybrid nanostructure with co-doped Co, Ni, and S on an N-enriched carbon polyhedron ($CoNi_xS_y$/NCP) electrocatalyst *via* absorption–pyrolysis–sulphuration of ZIF-67. Ni^{2+} is immersed in the pores of ZIF-67 and can be transmuted into $CoNi_xS_y$/NCP, which exhibits a potential as low as 1.51 V to achieve 10 mA cm^{-2} current density.[41] ZIF-8@$CoFe_2O_4$ composites synthesized by Yoo *et al.* with varying concentrations of $CoFe_2O_4$ were used as electrocatalysts in the methanol oxidation and the OER, among which ZCFO-1 exhibited a lower overpotential of 330 mV and a Tafel slope of 84 mV dec^{-1}.[42] Similarly, based on C–N frameworks, Yao's research team have demonstrated porphyrin-like Ru_1–N_4 mononuclear sites on graphite carbon nitride (g-C_3N_4) with an atomically dispersed structural configuration as a durable and competent electrocatalyst for the acidic OER, which demands a low overpotential of 267 mV at a current density of 10 mA cm^{-2}.[43]

Herein, we report a new method to trap atomically dispersed Ru sites on the molecular cages of ZnO for the first time using a two-step pyrolysis approach. The Ru single atomic sites openly coordinate with an electron-rich C–N skeleton. One of the effective strategies in molecular catalysis for enhancing the catalyst's performance is to alter the ligand coordination environment by tempering the active metal site with anions (N, P, S, *etc.*) of varying electronegativities. Thus, by tuning the donating/withdrawing properties of these anions, the transition kinetics intermediates and binding energies can be optimized. It was therefore believed that exploring anion-coordinated Ru_x-NC(ZnO) electrocatalysts would also effectually adjust the adsorption strength of OER intermediates at the active sites to further optimize the OER performance, which however has been seldom studied, let alone the precise alignment of coordination sites for anions as well as their ultimate influence on the OER. The best performing electrocatalyst $Ru_{1.75}$@NC(ZnO) demands overpotentials of 320, 372, and 410 mV to deliver current densities of 10, 15, and 20 mA cm^{-2} respectively for the OER.

Results and discussion

The incorporation of Ru SA sites in the NC(ZnO) nanostructure was achieved by a facile and simple two-time pyrolysis approach. The Ru^{+3} precursor ruthenium chloride hydrate was treated with an alcoholic dispersion of ZIF-derived ZnO template. The obtained product was then centrifuged and dried at 60 °C overnight. Afterwards, pyrolysis was carried out under an H_2/N_2 atmosphere in a 1 : 10 ratio at 250 °C for 2 h. The obtained sample was designated as Ru_x@NC(ZnO). The scheme of the synthetic procedure of Ru_x@NC(ZnO) is displayed in Fig. 1a.

The typical powder X-ray diffraction (XRD) patterns of the as-prepared samples are given in Fig. 1b. The XRD data agree well with the standard card of ZIF-8 (JCPDS No. 00-062-1030) and ZIF-8 derived ZnO (JCPDS No. 36-1451) with the previously reported XRD results. The diffraction peaks of NC(ZnO) and Ru_x@NC(ZnO) samples were precisely the same and sharp. For the NC(ZnO) composite, the diffraction peaks at 31.9°, 34.5°, and 36.40° are associated with (100), (002), and (101) planes respectively. From the XRD analysis, it is important to mention that no characteristic peak for the crystalline metallic Ru species was observed which indicates its atomically dispersed incorporation and ultra-low loading on the N rich carbon (NC) framework of ZnO. The high temperature annealing method incorporates the ZIF-8 into the highly porous host architecture towards the space confinement effect of ZnO by providing exposure to the active sites.

To learn more about the structure and morphology of the as-prepared composites, scanning electron and high-resolution transmission electron microscopy (SEM/HRTEM) techniques were exploited. The polyhedron morphology and crystalline structure of ZIF-8, and ZIF-8 derived ZnO, $Ru_{1.75}$@NC(ZnO) and Ru_3@NC(ZnO) are represented in Fig. S1a–d† as observed in SEM images. Heat treatment at an elevated temperature results in structural deformity up to some extent which can be observed in NC(ZnO) (Fig. 1c). The HRTEM picture obtained from the crystal lattices with a spacing of 0.25 nm matches with the (002) lattice plane of the ZnO crystal (Fig. 1d).[36] Furthermore, the selected area electron diffraction (SAED) pattern in Fig. 1e revealed further information about the crystalline makeup of the NC(ZnO) nanocrystal.

To further clearly expose the distribution and state of Ru at atomic resolution, high-angle annular dark-field-scanning transmission electron microscopy (HAADF-STEM) analysis was performed. HAADF analysis reveals the homogeneous distribution of Ru sites along with Zn and O elements observed on

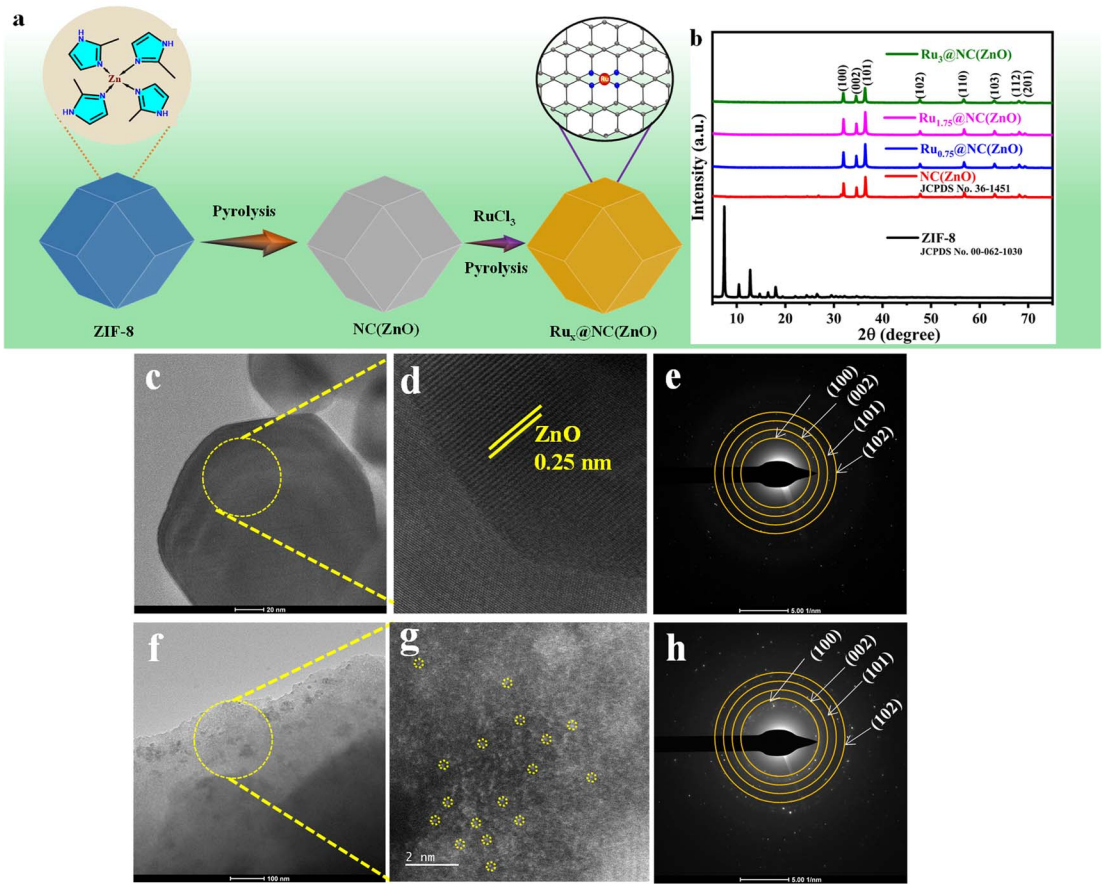

Fig. 1 (a) Schematic illustration of the preparation of the Ru_x@NC(ZnO) composite; (b) PXRD data of as-prepared samples; (c–e) HRTEM images and SAED pattern of NC(ZnO); (f) HRTEM image of $Ru_{1.75}$@NC(ZnO); (g) HAADF-STEM image of $Ru_{1.75}$@NC(ZnO); and (h) SAED pattern of $Ru_{1.75}$@NC(ZnO).

the NC rich ZnO matrix, which is provided in Fig. S2.† It is evident that there are a specific number of atom-sized bright spots, and the individual Ru atoms are dispersed all over the ZnO matrix, as indicated by the yellow circles, Fig. 1(f and g). Fig. 1h represents the SAED pattern of the $Ru_{1.75}$@NC(ZnO) composite. The loading amounts of Ru and Zn according to inductively coupled plasma-optical emission spectrometry (ICP-OES) measurements in $Ru_{1.75}$@NC(ZnO) were 0.8043 ppm and 52.20 ppm respectively (Table S2†) and the concentration of Zn in the NC(ZnO) was 74.43 ppm.

Surface water absorption is considered to be influenced by a solid surface's geometric architecture and chemical makeup. Photographs of surface contact angle measurements of electrocatalyst surfaces are displayed in Fig. S3.† The contact angles of 102.5°, 108.3°, and, 138.9° obtained for the $Ru_{1.75}$@NC(ZnO), ZIF-8, and, NC(ZnO) composites, respectively, highlight the hydrophobic nature of the materials as well as the surface interfacial charge separation and interaction of the surface with water and catalysts on their surfaces. The water contact angles of the $Ru_{1.75}$@NC(ZnO) electrocatalyst are noticeably smaller than those of the ZIF-8 and NC(ZnO), which may make it easier for electrons to reach the electrocatalyst's active surface. But for NC(ZnO), the rise in the water contact angle results from the fall in the particular increment owing to the reduction in the specific surface area of nanocages throughout the heat treatment.[44]

The Brunauer–Emmett–Teller (BET) surface area investigations at 77 K were used to determine the specific surface area, pore volume, and average pore diameter of ZIF-8, NC(ZnO), and $Ru_{1.75}$@NC(ZnO). The $Ru_{1.75}$@NC(ZnO) nanocomposite showed comparable hysteresis and isotherm to NC(ZnO) (Fig. S4a and b†). The values for surface area analyses are provided in Table S3.† In comparison to hexagonal NC(ZnO) nanostructures, the increased OER catalytic efficacy of $Ru_{1.75}$@NC(ZnO) is caused by mass/charge transfer towards reactant molecules, which is advantageous due to its greater surface area and highly porous structure.[45] It is important to note that as Ru sites on the matrix of the NC template are deposited, the mesoporous dimension may become blocked, which might account for the decrease in BET surface area.

The specific surface elemental composition and valence state related properties of Ru_x@NC(ZnO) electrocatalyst were further examined using X-ray photoelectron spectroscopy (XPS) analysis. As presented in Fig. S5a,† the coexistence of Ru, Zn, C, and O elements is shown in the XPS full survey spectrum of Ru_x@NC(ZnO). The C normalized 1s spectra of $Ru_{1.75}$@NC(ZnO) deconvoluted into C–C/C=C bonds (284.6 eV), C=C–N (285.2 eV), and N–C=N (288.7 eV) bonding in the NC(ZnO) matrix(Fig. 2a).[46] In Fig. S5c,† the N 1s peak at 390.6 eV is adjacent to the binding energy of the N–Zn bond as a distinctive peak.[47] Zn^{2+} was found to exist in $Ru_{1.75}$@NC(ZnO) through examination of the NC(ZnO) 2p XPS spectrum, with binding energies of 1024.1 and 1047.1 eV for the Zn $2p_{3/2}$ and Zn $2p_{1/2}$ peaks, respectively (Fig. 2b). In the O 1s XPS spectra of Ru1.75@NC(ZnO) (Fig. S5b†), besides the peak at 529.4 eV corresponding to Zn–O–Zn, a weak characteristic peak with BE of 536.3 eV was also observed which arose from oxygen vacancies introduced due to thermal H_2 treatment. In the Ru $3p_{3/2}$ XPS spectra, the peak at about 531.6 eV likely originated from RuOx due to the oxidation of Ru after exposure to air. An additional peak at 533 eV was also identified, possibly due to surface H_2O (adsorbed oxygen) because of the strong

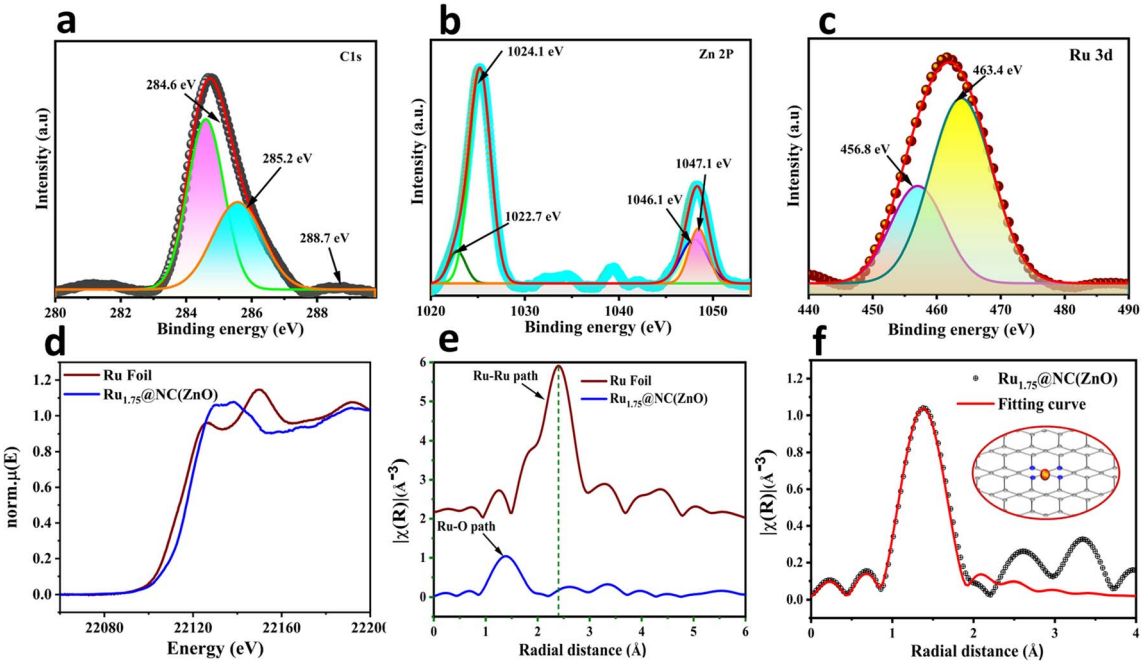

Fig. 2 High-resolution XPS spectra of (a) C 1s, (b) Zn 2p, and (c) Ru 3d, (d) XANES spectra of the sample measured at Ru K edge, (e) Fourier transformed EXAFS spectra of the sample measured at Ru K edge, and (f) EXAFS fitting curve for $Ru_{1.75}$@NC(ZnO).

hydrophilicity of oxygen vacancies. This peak confirms the existence of oxygen vacancies that arise from pyrolysis in an H_2 environment.[48] The deconvoluted Ru peak at 463.3 eV in Fig. 2c, which was attributed to electrons from the $3p_{3/2}$ orbital, confirmed the presence of Ru^{3+} in $Ru_{1.75}$@NC(ZnO).[49] By comparing the XPS study of Ru1.75@NC(ZnO) after and before the stability study all the characteristic peaks were observed to be intact, but a definite shift could be observed at 463.4 to 463.8 eV, *i.e.*, 0.4 eV which is due to the oxidation of Ru^{+2} to Ru^{+4} which acts as the active site for the OER.

Furthermore, the electronic and coordination structures of the $Ru_{1.75}$@NC(ZnO) electrocatalyst were studied with the X-ray absorption near-edge spectroscopy (XANES) and extended X-ray absorption fine structure (EXAFS) measurements. Fig. 2d shows the XANES spectra of the $Ru_{1.75}$@NC(ZnO) SAC sample at Ru K edge along with Ru Foil as the standard. In the Ru K-edge EXAFS spectrum of $Ru_{1.75}$@NC(ZnO), only a major peak at *ca.* 1.5 Å is noticed and no scattering from metallic Ru–Ru is evident (Fig. 2e).[48] At longer distances above 2.50 Å, no substantial involvement of metallic Ru, oxidized Ru_xO_y clusters, and $RuCl_3$ residuals were noticed, indicating the dispersion of isolated Ru atoms throughout the whole $Ru_{1.75}$@NC(ZnO) structure (Fig. 2e).[50,51] It shows the absence of a Ru–Ru path in the sample which indicates that all the Ru atoms in $Ru_{1.75}$@NC(ZnO) are in the single-atom form and are coordinated with oxygen. In the Fourier-transformed (FT) k^2-weighted EXAFS spectrum, one prominent peak was observed at $\approx$ 1.4 Å which was attributed to Ru–O bonds (Fig. 2f).

The Raman spectra of $Ru_{1.75}$@NC(ZnO) show a D-band ratio (approximately 1331 cm^{-1}) related to carbon defects and a G-band (approximately 1579 cm^{-1}), with a ratio of 1.02, as depicted in Fig. S6†. This ratio is greater than NC(ZnO) skeleton which reinforces the presence of more defects in the final composite. The sample $Ru_{1.75}$@NC(ZnO) displays Zn–N stretching at 421 cm^{-1} which represents the existence of the absorption peak of ZIF-8. After calcination, the imidazolate ring bands vanish, indicating a change in the ZIF-8 structure.

Electrocatalytic OER performance in acidic medium

The electrocatalytic studies of all the Ru_x@NC(ZnO) are tested in 0.5 M H_2SO_4 in a conventional three electrode system (see the ESI†). Linear sweep voltammetry (LSV) studies were conducted at a 5 mV s^{-1} scan rate and the obtained LSV polarization results of all the electrocatalysts are provided in Fig. 3a. The schematic presentation of the setup used for the investigation of the OER performance of the electrocatalysts is provided in Fig. 3f. The LSV polarization study (95% *iR* compensated) reveals that $Ru_{1.75}$@NC(ZnO) provides improved catalytic activity with an overpotential of 320 mV to achieve 10 mA cm^{-2} current density. Besides, Ru_3@NC(ZnO), $Ru_{0.75}$@NC(ZnO), NC(ZnO), and ZIF-8 deliver lower overpotentials of 348, 366, 400, and 427 mV to reach the same benchmark 10 mA cm^{-2} current density. For comparison, commercial RuO_2 has been taken which shows an overpotential of 349 mV to attain 10 mA cm^{-2} current density (Fig. S7†). Electrochemical impedance spectroscopy (EIS) was conducted to know the resistance for charge transfer at the electrode and electrolyte interface. Table S1† represents the impedance parameters obtained from the fitted equivalent circuit diagram. The EIS results in Fig. 3b demonstrate that, obviously, $Ru_{1.75}$@NC(ZnO) has exhibited less resistance

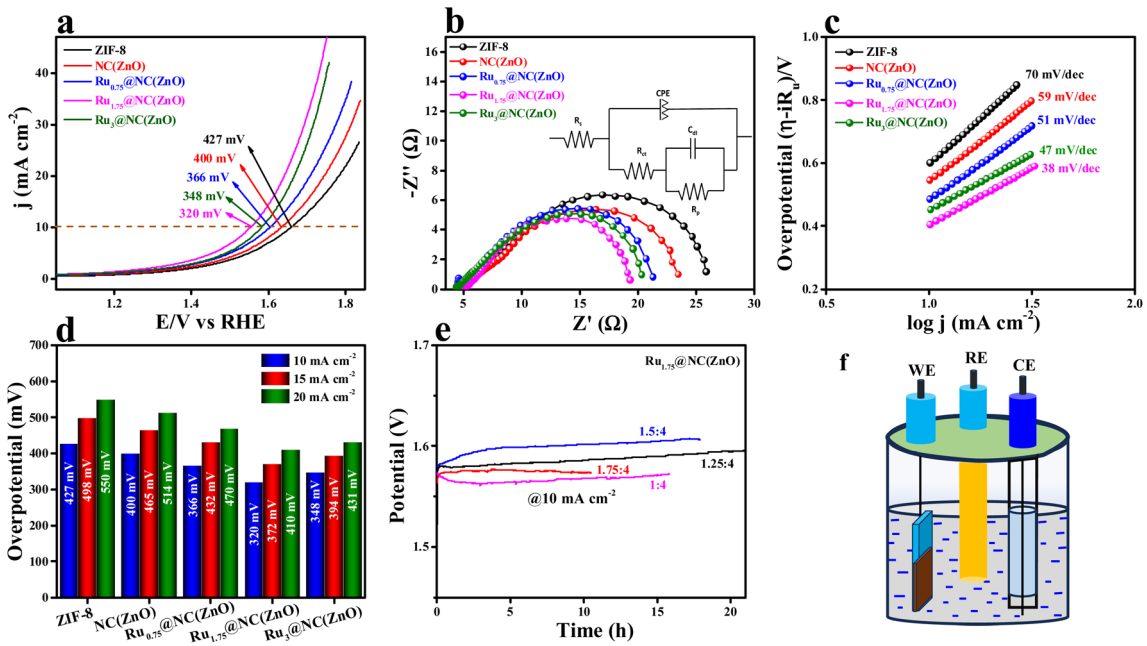

Fig. 3 (a) LSV polarization results of ZIF-8, NC(ZnO), $Ru_{0.75}$@NC(ZnO), $Ru_{1.75}$@NC(ZnO) and Ru_3@NC(ZnO); (b) EIS outcomes; the inset shows the equivalent circuit diagram; (c) *iR* drop free Tafel slope; (d) overpotential measured at different current densities; (e) long term-static stability at an applied current density of 10 mA cm^{-2}; (f) cell representation of the three-electrode setup used for OER performance.

towards electron transfer at the electrode–electrolyte interface with an R_{ct} value of 15.1 Ω, whereas Ru_3@NC(ZnO) (15.4 Ω), $Ru_{0.75}$@NC(ZnO) (16.9 Ω), NC(ZnO) (18.9 Ω), and ZIF-8 (20.9 Ω) show higher resistance than $Ru_{1.75}$@NC(ZnO). The inset of Fig. 3b displays the equivalent circuit diagram for the corresponding EIS curves. Furthermore, the Tafel slope was derived from the *iR* drop free LSV polarization outcomes and the obtained Tafel slope is given in Fig. 3c. These Tafel slopes suggest that $Ru_{1.75}$@NC(ZnO) delivers a very low Tafel slope value of 38 mV dec^{-1} compared to the other catalysts Ru_3@NC(ZnO) (47 mV dec^{-1}), $Ru_{0.75}$@NC(ZnO) (51 mV dec^{-1}), NC(ZnO) (59 mV dec^{-1}), and ZIF-8 (70 mV dec^{-1}) suggesting faster transfer kinetics at the electrode–electrolyte interface. The Tafel slope is a crucial kinetic parameter that signifies a change in the electron–proton–coupled transfer (OER) mechanism. The Tafel slope has been widely investigated in relation to the rate-determining step for OER electrocatalysis.[52–55] The chemical stages involved in the mechanism of the OER on the electrode's active metal oxide are often proposed to involve the following in acidic medium:

$$S + H_2O \rightarrow S\text{–}OH_{ads} + H^+ + e^- \quad (1)$$

$$S\text{–}OH_{ads} \rightarrow S\text{–}O_{ads} + H^+ + e^- \quad (2)$$

$$2S\text{–}O_{ads} \rightarrow S\text{–}O_{ads} + H_2O \quad (3)$$

$$S\text{–}O_{ads} \rightarrow S + 1/2O_2 \quad (4)$$

where S refers to the active sites on the oxide surface and S–OH_{ads} and S–O_{ads} correspond to the involved adsorption intermediates. According to the previous literature, the adsorption intermediates (S–OH_{ads}, S–O_{ads}) of step 3 and 4 are evidenced by the compact morphology and splintered morphology, respectively.[56] Among these steps, the rate determining step (RDS) was determined by Tafel slope values, where the Tafel slope largely depends on the physical properties and composition of the electrode. Moreover, these factors will moderately vary the adsorption intermediates during the OER process. Based on the previous reports, it is believed that if the Tafel slope value is higher than or equivalent to 120 mV dec^{-1}, the adsorption and formation of the first intermediate, S–OH_{ads}, is considered to be the RDS. If the Tafel slope is believed to be 40 mV dec^{-1} or more, conversion of S–OH_{ads} to S–O_{ads} will be the RDS, whereas if the Tafel slop is less than 40, the RDS will be the generation/liberation of O_2 molecules from the S–OH_{ads} intermediates.[57–59] Herein, we have observed that $Ru_{1.75}$@NC(ZnO) possesses a lower Tafel slope of 38 mV dec^{-1} suggesting that conversion of S–OH_{ads} to S–O_{ads} will be the RDS. Even though we have observed 70 mV dec^{-1} as the Tafel slope for our bare NC(ZnO) and suggest that the conversion of S–OH_{ads} to S–O_{ads} is the RDS, the synergistic effect between ZnO and the optimized amount of Ru will further expedite the conversion of S–OH_{ads} to S–O_{ads} intermediates which facilitates the OER process. Moreover, we measured the overpotential at different current densities (10, 15, and 20 mA cm^{-2}) and depicted as a bar diagram in Fig. 3d.

The bar diagram demonstrates that even at higher current densities the same activity trend was obtained ($Ru_{1.75}$@NC(ZnO) > Ru_3@NC(ZnO) > $Ru_{0.75}$@NC(ZnO) > NC(ZnO) > ZIF-8). To understand the long-term static stability of $Ru_{1.75}$@NC(ZnO), chronopotentiometric analysis (Fig. 3e) was performed where it showed a static stability for 21 h at an applied current density of 10 mA cm^{-2} with a binder and catalyst ratio of 1.25 : 4. These chronoamperometric studies suggest the highly stable nature in a highly harsh and corrosive environment. To further govern the intrinsic activity of all the catalysts, the turnover frequency (TOF) was calculated, which is nothing but the number of O_2 molecules evolved per unit area per second. The assessed TOF values are projected as a bar diagram in Fig. 4a with an error bar. The bar diagram demonstrates that $Ru_{1.75}$@NC(ZnO) possess higher TOF values of 2.8501×10^{-5} s^{-1}, whereas Ru_3@NC(ZnO), $Ru_{0.75}$@NC(ZnO), NC(ZnO), and ZIF-8 exhibit TOF values of 2.3060, 1.8150, 1.4652, and 1.2307×10^{-5} s^{-1} respectively. The higher TOF value of $Ru_{1.75}$@NC(ZnO) indicates that a larger number of O_2 molecules are liberated during the OER process than the residual catalyst. To know the reason behind the higher TOF value, electrical double-layered capacitance (C_{dl}) was determined by carrying out cyclic voltammetry (CV) between the applied potential of 1.0 and 1.2 V *vs.* RHE at different scan rates (Fig. S8a–e†). From the measured CVs, C_{dl} values are determined by subtracting the anodic–cathodic current with a linear fitting, and the outcomes are given in Fig. 4b. The determined C_{dl} values evidence that $Ru_{1.75}$@NC(ZnO) occupies a higher peak position (Fig. 4c) with a C_{dl} value of 0.0501 mF than other catalysts such as Ru_3@NC(ZnO) (0.0462 mF), $Ru_{0.75}$@NC(ZnO) (0.0429 mF), NC(ZnO) (0.0386 mF), and ZIF-8 (0.032 mF). The highest peak position indicates that $Ru_{1.75}$@NC(ZnO) exposes abundant active sites for the adsorption/desorption of H_2O/O_2 molecules than the residual catalyst. Furthermore, with the obtained C_{dl} values the electrochemical active surface areas (ECSAs) of all the catalysts were evaluated by employing the below formula: w

$$\mathrm{ECSA} = \frac{C_{dl}}{C_s} \quad (5)$$

here C_s is the specific capacitance of the flat electrode surface (0.04 mF cm^{-2}).[60] The obtained ECSA values of ZIF-8, NC(ZnO), $Ru_{0.75}$@NC(ZnO), $Ru_{1.75}$@NC(ZnO), and Ru_3@NC(ZnO) are 0.8075, 0.965, 1.0725, 1.2525, and 1.155 cm^2, respectively. The higher ECSA value again indicates that $Ru_{1.75}$@NC(ZnO) possesses numerous active sites for O_2 conversion. Furthermore, with the achieved ECSA values the specific activities of all the catalysts were evaluated and the results are provided in Fig. 4d. After normalizing the ECSA values with the geometrical LSV results, a similar activity trend was observed with an overpotential of 336, 358, 377, 398, and 406 mV corresponding to $Ru_{1.75}$@NC(ZnO), Ru_3@NC(ZnO), $Ru_{0.75}$@NC(ZnO), NC(ZnO), and ZIF-8 to attain 10 mA cm^{-2} current density respectively. Later, the mass dependent activity of all the catalysts was also determined by dividing the catalyst loading with the obtained current density, and the obtained values are given in Fig. 4e.

The mass-dependent results showed an overpotential of 322, 355, 370, 382, and 410 mV corresponding to $Ru_{1.75}$@NC(ZnO),

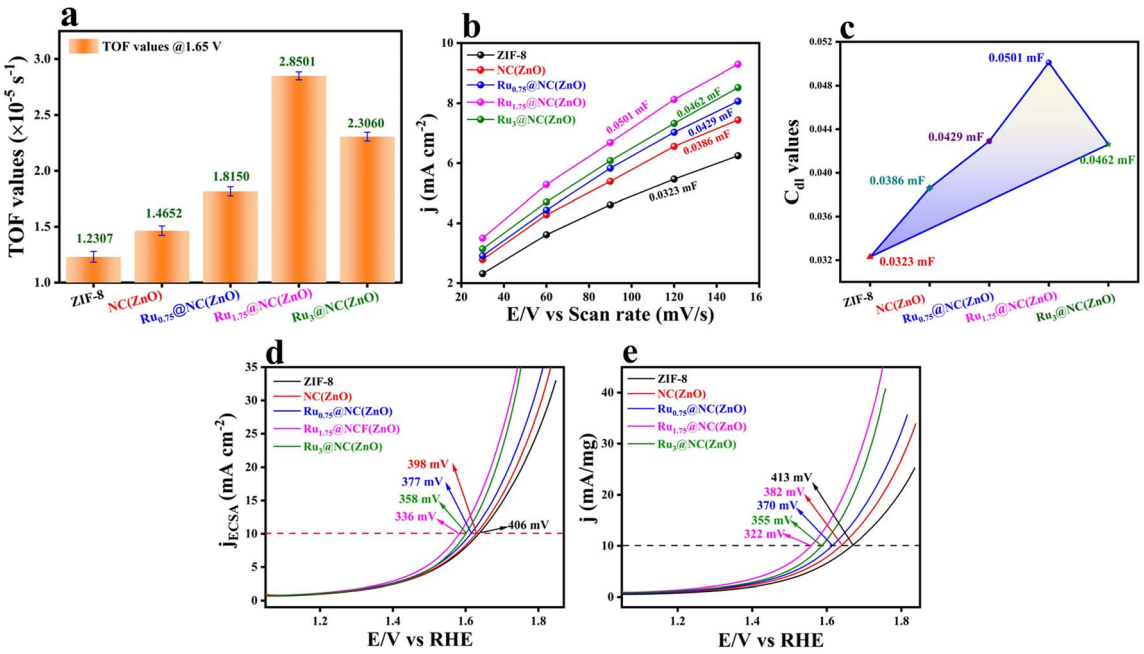

Fig. 4 (a) TOF values of ZIF-8, NC(ZnO), $Ru_{0.75}$@NC(ZnO), $Ru_{1.75}$@NC(ZnO)and Ru_3@NC(ZnO); (b) C_{dl} values measured from the CV curves; (c) comparison of the C_{dl} values; (d) ECSA normalized (specific activity) LSV polarization results; (e) mass dependent activity of all the catalysts.

Ru_3@NC(ZnO), $Ru_{0.75}$@NC(ZnO), NC(ZnO), and ZIF-8 to reach the same current density. Additionally, operando-EIS analysis was executed at several potentials to comprehend the electron transport kinetics at the electrode–electrolyte boundary and the obtained Nyquist plots are given in Fig. S9a–d.† The Nyquist plots of all the electrocatalysts exhibit promising electrochemical performances. Moreover, the Bode plot was also recorded and is shown in Fig. 5a–d. The regions of the Bode plot represent the reagent (OH^-) that has been adsorbed or desorbed on the electrode surface. The high-frequency zone (HF) detects the oxidation of the electrocatalyst, whereas the low-frequency zone (LF) reveals the unequal distribution of the oxidising agent at the electrode interface. Fig. 5e demonstrates that, at an applied potential of 1.52 V *vs.* RHE, the phase angle was decreased at the HF region,

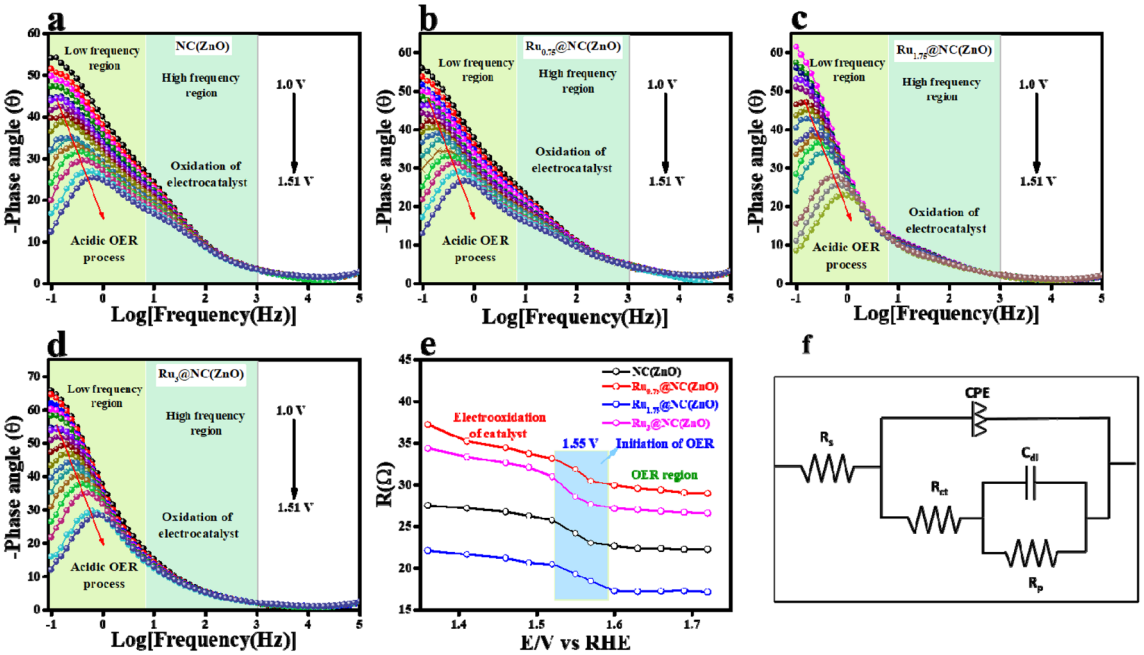

Fig. 5 (a–d) Operando Bode plot of NC(ZnO), $Ru_{0.75}$@NC(ZnO), $Ru_{1.75}$@NC(ZnO) and Ru_3@NC(ZnO); (e) correlation of the equivalent resistances and potentials for the electrodes and mass dependent activity of all the catalysts. (f) Equivalent circuit diagram used for fitting the impedance data.

suggesting the electrooxidation of the catalyst, whereas at a 1.55 V (*vs.* RHE) applied voltage, evolution of oxygen will begin. Fig. 5f represents the equivalent circuit diagram of the corresponding OER process. Faradaic efficiency (FE) was computed to compare the calculated and actual quantities of oxygen evolved in order to assess the selectivity towards the oxygen redox reaction.

Fig. S10† shows that the predicted faradaic efficiency for $Ru_{1.75}$@NC(ZnO) was 91.02%, indicating a higher selectivity towards the OER. Moreover, the robustness of the catalyst $Ru_{1.75}$@NC(ZnO) was confirmed by performing 500 CV cycles at a scan rate of 150 mV s^{-1} in an acidic environment. After 500 CV cycles, LSV was recorded at 5 mV s^{-1} scan rate and the results are provided in Fig. S11a.† After continuous CV cycling the activity of $Ru_{1.75}$@NC(ZnO) decreased with a change of 30 mV to attain 10 mA cm^{-2} current density. This decrease in activity might be due to that with the continuous CV cycling the charge accumulated over the electrode surface might be reduced, which simultaneously leads to reduction in the conversion of O_2 molecules. The corresponding EIS analysis in Fig. S11b† also shows the same results which well agreed with the LSV results. Overall, from the above results it appears to be a promising electrocatalyst for the OER in acidic media, demonstrating superior catalytic performance, low overpotential, faster electron transfer kinetics, and reasonable stability. Moreover, after chronopotentiometric studies, the electrode was subjected to chemical nature analysis, *i.e.*, XPS analysis (Fig. S13†) and morphological analysis (Fig. S14†). Fig. S14a and b† represent the P-XRD and SEM images of the $Ru_{1.75}$@NC(ZnO) catalyst respectively after OER activity, both of which reveal that the catalyst does not lose its robust nature after the catalytic performance. By comparing the XPS study of $Ru_{1.75}$@NC(ZnO) after and before the stability study all the characteristic peaks were observed to be intact, but a definite shift could be observed from 463.4 to 463.8 eV, *i.e.* 0.4 eV, which is due to the oxidation of Ru^{+2} to Ru^{+4} which acts as the active site for the OER.

Computational study

Results and discussion

We carried out DFT calculations to get the atomic-scale insights into the improved OER performance of Ru_x@NC(ZnO). To complement our experimental results, we performed the adsorption of Ru loaded ZnO (Ru@ZnO) on the optimized nitrogen-doped porous carbon matrix (NC) to obtain the

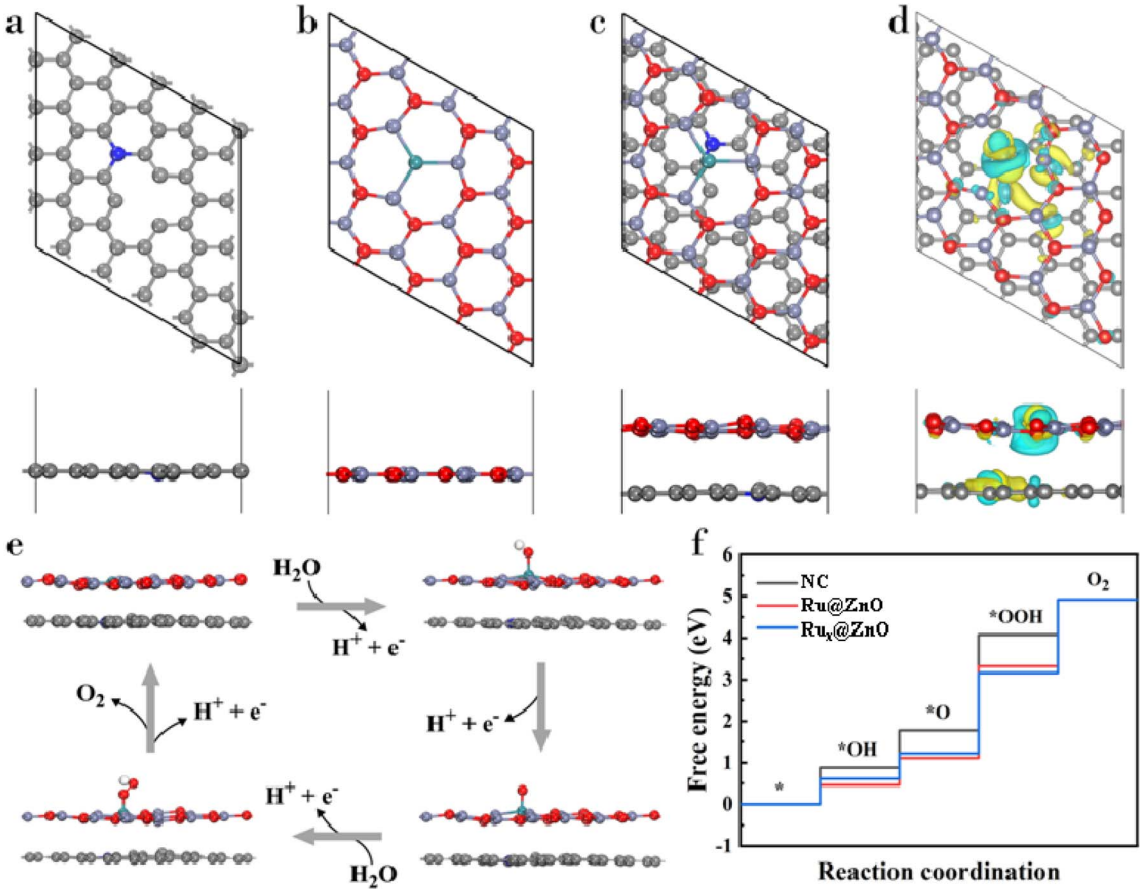

Fig. 6 Top view and side view of the optimized structures of (a) NC, (b) Ru_x@ZnO and (c) Ru@NC(ZnO). (d) Charge density difference for the Ru_x@NC(ZnO) complex. Here, blue and yellow isosurfaces indicate charge depletion and accumulation, respectively. (e) Proposed $4e^-$ mechanism of the oxygen evolution reaction along with the optimized structures of Ru_x@NC(ZnO). The balls in red, purple, blue, grey, green and white represent O, Zn, N, C, Ru, and H atoms, respectively. (f) The DFT computed adsorption free energy profiles of the OER process on NC, Ru@ZnO and Ru_x@NC(ZnO) at $U = 0$ eV.

Ru_x@NC(ZnO) complex as shown in Fig. 6a–c. Using the charge density difference (CDD) plot, we analysed the charge distribution between Ru–ZnO and NC layers. As shown in Fig. 6d, the yellow area demonstrates an accumulation of charge suggesting an increase in electron density within Ru–ZnO, where the Ru atom plays a significant role in this effect. On the other hand, a decrease in the electron density within NC is evident from the blue region, indicating a depletion of charge. The observation suggests the presence of a built-in electric field that potentially facilitates the transfer of electrons at the interface.

In the acidic environment, the typical OER process can be expressed by the following four elementary reaction paths:

$$H_2O(l) + * \rightarrow *OH + (H^+ + e^-) \quad (6)$$

$$*OH \rightarrow *O + (H^+ + e^-) \quad (7)$$

$$*O + H_2O(l) \rightarrow *OOH + (H^+ + e^-) \quad (8)$$

$$*OOH \rightarrow * + O_2(g) + (H^+ + e^-) \quad (9)$$

Here, (l), (g), and * denote the liquid phase, gas phase, and an active site on the catalyst surface, respectively, while *OH, *O, and *OOH represent adsorbed intermediates. Fig. 6e represents the adsorption configurations of the intermediate species of the Ru_x@NC(ZnO) complex. To assess the OER activities of NC, Ru@ZnO and Ru_x@NC(ZnO) catalysts, we investigated the free energies of OER intermediates. The free energy change for the initial step ($H_2O \rightarrow *OH$) in the OER on NC is determined to be 0.93 eV, indicating the challenging decomposition of the water molecule, while in Ru@ZnO and Ru_x@NC(ZnO), the free energy change for the first step ($H_2O \rightarrow *OH$) is 0.45 and 0.56 eV, making water dissociation significantly easier. The potential-determining step (PDS) for all cases is the formation of *OOH ($*O \rightarrow *OOH$) with a ΔG_3 value of 2.32 (overpotential of 1.08 V) and 2.20 eV (overpotential of 0.97 V) for NC and Ru@ZnO, respectively. In Ru_x@NC(ZnO), the overpotential is reduced to 0.71 eV with a ΔG_3 value of 1.95 eV (Fig. 6f), revealing the origin of the increased OER activity. Therefore, a forward shift in the PDS, coupled with a lowered free energy indicates the crucial role of Ru in enhancing the OER activity of the Ru_x@NC(ZnO) catalyst. These results exhibited a strong agreement with the experimental OER activity data, emphasizing the significant contribution of Ru loading in NC(ZnO) to the enhancement of catalytic performance. As shown in Fig. S15,† the yellow region demonstrates an accumulation of charge suggesting an increase in electron density within Ru–ZnO, where the Ru atom plays a significant role in this effect. On the other hand, the decrease in the electron density within CN is indicated by the blue region, indicating a depletion of charge. The observation suggests the presence of a built-in electric field that potentially facilitates the transfer of electrons at the interface.

Conclusion

In summary, we designed and synthesized atomically scattered Ru sites on the NC(ZnO) nanocage architecture under mild conditions and employed them for the OER in an acidic environment. The resulting atomically regulated $Ru_{1.75}$@NC(ZnO) electrocatalyst, featuring an abundance of active sites, emerged as a promising candidate for the OER. It exhibited superior catalytic performance, low overpotential, accelerated electron transfer kinetics, and reasonable stability. $Ru_{1.75}$@NC(ZnO) shows a low overpotential (320 mV) at a current density of 10 mA cm^{-2} for the OER because of the high active site utilisation. The feasibility of the OER process by employing Ru_x@NC(ZnO) was also established from DFT studies which divulges the formation of *OH, *O, and *OOH intermediates with lower free energy in the water decomposition process. This research provides a systematic guideline illustrating the synergistic interaction between Ru atomic sites and ZnO derived from the ZIF-8 framework. It elucidates how this collaborative interaction can be harnessed to enhance the electrocatalytic performance. The concepts presented in this study are poised to open avenues for the development of atom regulated catalysts that are both durable and exceptionally active for electrocatalysis of water to store energy.

Data availability

The data that support the findings of this study are available from the corresponding author upon reasonable request.

Conflicts of interest

The authors declare no conflict of interest.

Acknowledgements

S. V.; R. M.; S. M.; and B. J.; are thankful to AcSIR for their PhD enrolment. S. V. acknowledges his financial support from CSIR-IICT, Hyderabad (project code: HCP-0023). The authors thank DST HFC (GAP-0820) research grants (project no. DST/TMD/HFC/2K18/60/(C)/3) Government of India for financial support. The authors are thankful to Dr D. Srinivasa Reddy, Director, Dr A. Gangagni Rao, HOD, DEEE division in CSIR-IICT (www.iict.res.in) for providing all research facilities. B. M. A. would like to thank Spanish MICIUN for the Juan de la Cierva Formación grant (FJC2021-047213-I). CSIR-IICT Communication IICT/Pubs./2024/006.

Notes and references

1 W. Xie, Y. Song, S. Li, J. Li, Y. Yang, W. Liu, M. Shao and M. Wei, Single-Atomic-Co Electrocatalysts with Self-Supported Architecture toward Oxygen-Involved Reaction, *Adv. Funct. Mater.*, 2019, **29**(50), 1906477, DOI: 10.1002/adfm.201906477.

2 M. Moses-Debusk, M. Yoon, L. F. Allard, D. R. Mullins, Z. Wu, X. Yang, G. Veith, G. M. Stocks and C. K. Narula, CO Oxidation on Supported Single Pt Atoms: Experimental and Ab Initio Density Functional Studies of CO Interaction with Pt Atom on θ-Al 2O3(010) Surface, *J. Am. Chem. Soc.*, 2013, **135**(34), 12634–12645, DOI: 10.1021/ja401847c.

3 R. Zeng, M. Feller, Y. Diskin-Posner, L. J. W. Shimon, Y. Ben-David and D. Milstein, CO Oxidation by N2O Homogeneously Catalyzed by Ruthenium Hydride Pincer Complexes Indicating a New Mechanism, *J. Am. Chem. Soc.*, 2018, **140**(23), 7061–7064, DOI: 10.1021/jacs.8b03927.

4 H. Yan, Y. Lin, H. Wu, W. Zhang, Z. Sun, H. Cheng, W. Liu, C. Wang, J. Li, X. Huang, T. Yao, J. Yang, S. Wei and J. Lu, Bottom-up Precise Synthesis of Stable Platinum Dimers on Graphene, *Nat. Commun.*, 2017, **8**(1), 1070, DOI: 10.1038/s41467-017-01259-z.

5 S. Tong, X. Gao, H. Zhou, Q. Shi, Y. Wu and W. Chen, Synergistic Roles of the CoO/Co Heterostructure and Pt Single Atoms for High-Efficiency Electrocatalytic Hydrogenation of Lignin-Derived Bio-Oils, *Inorg. Chem.*, 2023, **62**(46), 19123–19134, DOI: 10.1021/acs.inorgchem.3c03338.

6 J. Li, Q. Guan, H. Wu, W. Liu, Y. Lin, Z. Sun, X. Ye, X. Zheng, H. Pan, J. Zhu, S. Chen, W. Zhang, S. Wei and J. Lu, Highly Active and Stable Metal Single-Atom Catalysts Achieved by Strong Electronic Metal–Support Interactions, *J. Am. Chem. Soc.*, 2019, **141**(37), 14515–14519, DOI: 10.1021/jacs.9b06482.

7 M. Mokhtarnejad, E. L. Ribeiro, D. Mukherjee and B. Khomami, Facile Synthesis of Nonprecious Bimetallic Zeolitic Imidazolate Framework-Based Hierarchical Nanocomposites as Efficient Electrocatalysts for Oxygen Reduction Reaction, *ACS Appl. Nano Mater.*, 2023, **6**(14), 13698–13707, DOI: 10.1021/acsanm.3c02703.

8 X. Xie, Y. Fan, W. Tian, M. Zhang, J. Cai, X. Zhang, J. Ding, Y. Liu and S. Lu, Construction of Ru/WO3 with Hetero-Interface Structure for Efficient Hydrogen Evolution Reaction, *J. Energy Chem.*, 2023, **83**, 150–157, DOI: 10.1016/j.jechem.2023.04.026.

9 N. Akbari, S. Nandy, K. H. Chae and M. M. Najafpour, Unraveling the Dynamic Behavior of Iron-Doped Oxidized Cobalt–Nickel Alloy in the Oxygen-Evolution Reaction, *ACS Appl. Energy Mater.*, 2023, **6**(22), 11613–11625, DOI: 10.1021/acsaem.3c02012.

10 Q. Y. Li, L. Zhang, Y. X. Xu, Q. Li, H. Xue and H. Pang, Smart Yolk/Shell ZIF-67@POM Hybrids as Efficient Electrocatalysts for the Oxygen Evolution Reaction, *ACS Sustain. Chem. Eng.*, 2019, **7**(5), 5027–5033, DOI: 10.1021/acssuschemeng.8b05744.

11 S. K. Kaiser, Z. Chen, D. Faust Akl, S. Mitchell and J. Pérez-Ramírez, Single-Atom Catalysts across the Periodic Table, *Chem. Rev.*, 2020, **120**(21), 11703–11809, DOI: 10.1021/acs.chemrev.0c00576.

12 X. Yang, B. Ouyang, L. Zhao, Q. Shen, G. Chen, Y. Sun, C. Li and K. Xu, Ultrathin Rh Nanosheets with Rich Grain Boundaries for Efficient Hydrogen Oxidation Electrocatalysis, *J. Am. Chem. Soc.*, 2023, **145**(49), 27010–27021, DOI: 10.1021/jacs.3c10465.

13 C. Hu, F. Wei, Q. Liang, Q. Peng, Y. Yang, T. Taylor Isimjan and X. Yang, Electronically Modulated D-Band Centers of MOF-Derived Carbon-Supported Ru/HfO2 for Oxygen Reduction and Aqueous/Flexible Zinc-Air Batteries, *J. Energy Chem.*, 2023, **80**, 247–255, DOI: 10.1016/j.jechem.2023.01.047.

14 S. Ghosh, P. Kar, N. Bhandary, S. Basu, T. Maiyalagan, S. Sardar and S. K. Pal, Reduced Graphene Oxide Supported Hierarchical Flower like Manganese Oxide as Efficient Electrocatalysts toward Reduction and Evolution of Oxygen, *Int. J. Hydrogen Energy*, 2017, **42**(7), 4111–4122, DOI: 10.1016/j.ijhydene.2016.12.008.

15 F.-F. Zhang, C.-Q. Cheng, J.-Q. Wang, L. Shang, Y. Feng, Y. Zhang, J. Mao, Q.-J. Guo, Y.-M. Xie, C.-K. Dong, Y.-H. Cheng, H. Liu and X.-W. Du, Iridium Oxide Modified with Silver Single Atom for Boosting Oxygen Evolution Reaction in Acidic Media, *ACS Energy Lett.*, 2021, **6**(4), 1588–1595, DOI: 10.1021/acsenergylett.1c00283.

16 Q. Shi, C. Zhu, D. Du and Y. Lin, Robust Noble Metal-Based Electrocatalysts for Oxygen Evolution Reaction, *Chem. Soc. Rev.*, 2019, **48**(12), 3181–3192, DOI: 10.1039/C8CS00671G.

17 T. Pan, J. Alvarado, J. Zhu, Y. Yue, H. L. Xin, D. Nordlund, F. Lin and M. M. Doeff, Structural Degradation of Layered Cathode Materials in Lithium-Ion Batteries Induced by Ball Milling, *J. Electrochem. Soc.*, 2019, **166**(10), A1964–A1971, DOI: 10.1149/2.0091910jes.

18 Y. Wang, R. Ma, K. Hu, S. Kim, G. Fang, Z. Shao and V. V. Tsukruk, Dramatic Enhancement of Graphene Oxide/Silk Nanocomposite Membranes: Increasing Toughness, Strength, and Young's Modulus via Annealing of Interfacial Structures, *ACS Appl. Mater. Interfaces*, 2016, **8**(37), 24962–24973, DOI: 10.1021/acsami.6b08610.

19 A. Mardana, M. Bai, A. Baruth, S. Ducharme and S. Adenwalla, Magnetoelectric Effects in Ferromagnetic Cobalt/Ferroelectric Copolymer Multilayer Films, *Appl. Phys. Lett.*, 2010, **97**(11), 112904, DOI: 10.1063/1.3488814.

20 Y. Jiao, Y. Zheng, M. Jaroniec and S. Z. Qiao, Design of Electrocatalysts for Oxygen- and Hydrogen-Involving Energy Conversion Reactions, *Chem. Soc. Rev.*, 2015, **44**(8), 2060–2086, DOI: 10.1039/c4cs00470a.

21 E. Saha, K. Karthick, S. Kundu and J. Mitra, Electrocatalytic Oxygen Evolution in Acidic and Alkaline Media by a Multistimuli-Responsive Cobalt(II) Organogel, *ACS Sustain. Chem. Eng.*, 2019, **7**(19), 16094–16102, DOI: 10.1021/acssuschemeng.9b02858.

22 Y. Liao, Y. Xiao, Z. Li, X. Zhou, J. Liu, F. Guo, J. Li and Y. Li, Structural Engineering of Co-Metal–Organic Frameworks via Ce Incorporation for Improved Oxygen Evolution, *Small*, 2023, 2307685, DOI: 10.1002/smll.202307685.

23 S. Sk, R. Madhu, D. S. Gavali, V. Bhasin, R. Thapa, S. N. Jha, D. Bhattacharyya, S. Kundu and U. Pal, An Ultrathin 2D NiCo-LDH Nanosheet Decorated NH2-UiO-66 MOF-Nanocomposite with Exceptional Chemical Stability for Electrocatalytic Water Splitting, *J. Mater. Chem. A*, 2023, **11**(19), 10309–10318, DOI: 10.1039/D3TA00836C.

24 H. Jungi, A. Karmakar, S. Kundu and J. Mitra, Waste Is the Best: End-of-Life Lithium Ion Battery-Derived Ultra-Active Ni3+-Enriched β-Ni(OH)2 for the Electrocatalytic Oxygen Evolution Reaction, *J. Mater. Chem. A*, 2023, **11**(25), 13687–13696, DOI: 10.1039/D3TA01989F.

25 Y. Zhao, M. Xi, Y. Qi, X. Sheng, P. Tian, Y. Zhu, X. Yang, C. Li and H. Jiang, Redirecting Dynamic Structural Evolution of Nickel-Contained RuO2 Catalyst during Electrochemical

Oxygen Evolution Reaction, *J. Energy Chem.*, 2022, **69**, 330–337, DOI: 10.1016/j.jechem.2022.01.030.

26 Y. Shi, H. Wu, J. Chang, Z. Tang and S. Lu, Progress on the Mechanisms of Ru-Based Electrocatalysts for the Oxygen Evolution Reaction in Acidic Media, *J. Energy Chem.*, 2023, **85**, 220–238, DOI: 10.1016/j.jechem.2023.06.001.

27 A. Meena, P. Thangavel, D. S. Jeong, A. N. Singh, A. Jana, H. Im, D. A. Nguyen and K. S. Kim, Crystalline-Amorphous Interface of Mesoporous Ni2P @ FePOxHy for Oxygen Evolution at High Current Density in Alkaline-Anion-Exchange-Membrane Water-Electrolyzer, *Appl. Catal., B*, 2022, **306**, 121127, DOI: 10.1016/j.apcatb.2022.121127.

28 G. Yasin, S. Ali, S. Ibraheem, A. Kumar, M. Tabish, M. A. Mushtaq, S. Ajmal, M. Arif, M. A. Khan, A. Saad, L. Qiao and W. Zhao, Simultaneously Engineering the Synergistic-Effects and Coordination-Environment of Dual-Single-Atomic Iron/Cobalt-Sites as a Bifunctional Oxygen Electrocatalyst for Rechargeable Zinc-Air Batteries, *ACS Catal.*, 2023, **13**(4), 2313–2325, DOI: 10.1021/acscatal.2c05654.

29 S. Ghosh, P. Kar, N. Bhandary, S. Basu, S. Sardar, T. Maiyalagan, D. Majumdar, S. K. Bhattacharya, A. Bhaumik, P. Lemmens and S. K. Pal, Microwave-Assisted Synthesis of Porous Mn2O3 Nanoballs as Bifunctional Electrocatalyst for Oxygen Reduction and Evolution Reaction, *Catal. Sci. Technol.*, 2016, **6**(5), 1417–1429, DOI: 10.1039/C5CY01264C.

30 M. Tavakkoli, E. Flahaut, P. Peljo, J. Sainio, F. Davodi, E. V. Lobiak, K. Mustonen and E. I. Kauppinen, Mesoporous Single-Atom-Doped Graphene–Carbon Nanotube Hybrid: Synthesis and Tunable Electrocatalytic Activity for Oxygen Evolution and Reduction Reactions, *ACS Catal.*, 2020, **10**(8), 4647–4658, DOI: 10.1021/acscatal.0c00352.

31 D. Narváez-Celada and A. S. Varela, CO2 Electrochemical Reduction on Metal–Organic Framework Catalysts: Current Status and Future Directions, *J. Mater. Chem. A*, 2022, **10**(11), 5899–5917, DOI: 10.1039/D1TA10440C.

32 S. Varangane, T. P. Yendrapati, A. Tripathi, R. Thapa, S. Bojja, P. Anand, V. Perupogu and U. Pal, Integrating Ultrasmall Pd NPs into Core–Shell Imidazolate Frameworks for Photocatalytic Hydrogen and MeOH Production, *Inorg. Chem.*, 2023, **62**(19), 7235–7249, DOI: 10.1021/acs.inorgchem.2c04524.

33 D. Zhao, Z. Zhuang, X. Cao, C. Zhang, Q. Peng, C. Chen and Y. Li, Atomic Site Electrocatalysts for Water Splitting, Oxygen Reduction and Selective Oxidation, *Chem. Soc. Rev.*, 2020, **49**(7), 2215–2264, DOI: 10.1039/C9CS00869A.

34 S. Varangane, A. Jamma, Y. T. Prabhu, A. Karmakar, S. Kundu, A. Tripathi, R. Thapa, V. Bhasin, S. N. Jha, D. Bhattacharyya and U. Pal, Pd Encapsulated Core-Shell ZIF-8/ZIF-67 for Efficient Oxygen Evolution Reaction, *Electrochim. Acta*, 2023, **447**, 142100, DOI: 10.1016/j.electacta.2023.142100.

35 X. Zeng, J. Shui, X. Liu, Q. Liu, Y. Li, J. Shang, L. Zheng and R. Yu, Single-Atom to Single-Atom Grafting of Pt1 onto Fe–N4 Center: Pt1@Fe–N–C Multifunctional Electrocatalyst with Significantly Enhanced Properties, *Adv. Energy Mater.*, 2018, **8**(1), 1701345, DOI: 10.1002/aenm.201701345.

36 A. Gautam, S. Sk and U. Pal, Recent Advances in Solution Assisted Synthesis of Transition Metal Chalcogenides for Photo-Electrocatalytic Hydrogen Evolution, *Phys. Chem. Chem. Phys.*, 2022, **24**(35), 20638–20673, DOI: 10.1039/D2CP02089K.

37 S. Ji, Y. Chen, X. Wang, Z. Zhang, D. Wang and Y. Li, Chemical Synthesis of Single Atomic Site Catalysts, *Chem. Rev.*, 2020, **120**(21), 11900–11955, DOI: 10.1021/acs.chemrev.9b00818.

38 M. Xiao, L. Gao, Y. Wang, X. Wang, J. Zhu, Z. Jin, C. Liu, H. Chen, G. Li, J. Ge, Q. He, Z. Wu, Z. Chen and W. Xing, Engineering Energy Level of Metal Center: Ru Single-Atom Site for Efficient and Durable Oxygen Reduction Catalysis, *J. Am. Chem. Soc.*, 2019, **141**(50), 19800–19806, DOI: 10.1021/jacs.9b09234.

39 J. Yang, B. Chen, X. Liu, W. Liu, Z. Li, J. Dong, W. Chen, W. Yan, T. Yao, X. Duan, Y. Wu and Y. Li, Efficient and Robust Hydrogen Evolution: Phosphorus Nitride Imide Nanotubes as Supports for Anchoring Single Ruthenium Sites, *Angew. Chem.*, 2018, **130**(30), 9639–9644, DOI: 10.1002/ange.201804854.

40 S. Liu, Z. Wang, S. Zhou, F. Yu, M. Yu, C.-Y. Chiang, W. Zhou, J. Zhao and J. Qiu, Metal–Organic-Framework-Derived Hybrid Carbon Nanocages as a Bifunctional Electrocatalyst for Oxygen Reduction and Evolution, *Adv. Mater.*, 2017, **29**(31), 1700874, DOI: 10.1002/adma.201700874.

41 Y. Zheng, L. Zhang, H. Huang, F. Wang, L. Yin, H. Jiang, D. Wang, J. Yang and G. Zuo, ZIF-67-Derived Co, Ni and S Co-Doped N-Enriched Porous Carbon Polyhedron as an Efficient Electrocatalyst for Oxygen Evolution Reaction (OER), *Int. J. Hydrogen Energy*, 2019, **44**(50), 27465–27471, DOI: 10.1016/j.ijhydene.2019.08.227.

42 T. V. M. Sreekanth, K. Prasad, J. Yoo, J. Kim and K. Yoo, ZIF-8@CoFe2O4 as a Highly Efficient Bifunctional Electrocatalyst for the Methanol Oxidation and Oxygen Evolution Reactions, *Catal. Sci. Technol.*, 2023, **13**(11), 3445–3455, DOI: 10.1039/D3CY00378G.

43 L. Cao, Q. Luo, J. Chen, L. Wang, Y. Lin, H. Wang, X. Liu, X. Shen, W. Zhang, W. Liu, Z. Qi, Z. Jiang, J. Yang and T. Yao, Dynamic Oxygen Adsorption on Single-Atomic Ruthenium Catalyst with High Performance for Acidic Oxygen Evolution Reaction, *Nat. Commun.*, 2019, **10**(1), 4849, DOI: 10.1038/s41467-019-12886-z.

44 C. Liu, Y. Qiu, F. Wang, K. Wang, Q. Liang and Z. Chen, Design of Core–Shell-Structured ZnO/ZnS Hybridized with Graphite-Like C3N4 for Highly Efficient Photoelectrochemical Water Splitting, *Adv. Mater. Interfaces*, 2017, **4**(21), 1700681, DOI: 10.1002/admi.201700681.

45 C. S. Vennapoosa, S. Varangane, B. M. Abraham, V. Bhasin, S. Bhattacharyya, X. Wang, U. Pal and D. Chatterjee, Single-Atom Ru Catalyst-Decorated CNF(ZnO) Nanocages for Efficient H2 Evolution and CH3OH Production, *J. Phys. Chem. Lett.*, 2023, **14**(50), 11400–11411, DOI: 10.1021/acs.jpclett.3c02347.

46 J. Qin, H. Liu, P. Zou, R. Zhang, C. Wang and H. L. Xin, Altering Ligand Fields in Single-Atom Sites through Second-Shell Anion Modulation Boosts the Oxygen Reduction Reaction, *J. Am. Chem. Soc.*, 2022, **144**(5), 2197–2207, DOI: **10.1021/jacs.1c11331**.

47 H. Zhang, C. Kong, W. Li, G. Qin, H. Ruan and M. Tan, The Formation Mechanism and Stability of P-Type N-Doped Zn-Rich ZnO Films, *J. Mater. Sci.: Mater. Electron.*, 2016, **27**(5), 5251–5258, DOI: **10.1007/s10854-016-4421-9**.

48 S. Liu, Y. Wang, S. Wang, M. You, S. Hong, T. S. Wu, Y. L. Soo, Z. Zhao, G. Jiang, J. Qiu, B. Wang and Z. Sun, Photocatalytic Fixation of Nitrogen to Ammonia by Single Ru Atom Decorated TiO 2 Nanosheets, *ACS Sustain. Chem. Eng.*, 2019, **7**(7), 6813–6820, DOI: **10.1021/acssuschemeng.8b06134**.

49 C. Zhang, J. Sha, H. Fei, M. Liu, S. Yazdi, J. Zhang, Q. Zhong, X. Zou, N. Zhao, H. Yu, Z. Jiang, E. Ringe, B. I. Yakobson, J. Dong, D. Chen and J. M. Tour, Single-Atomic Ruthenium Catalytic Sites on Nitrogen-Doped Graphene for Oxygen Reduction Reaction in Acidic Medium, *ACS Nano*, 2017, **11**(7), 6930–6941, DOI: **10.1021/acsnano.7b02148**.

50 Z. Geng, Y. Liu, X. Kong, P. Li, K. Li, Z. Liu, J. Du, M. Shu, R. Si and J. Zeng, Achieving a Record-High Yield Rate of 120.9 for N2 Electrochemical Reduction over Ru Single-Atom Catalysts, *Adv. Mater.*, 2018, **30**(40), 1803498, DOI: **10.1002/adma.201803498**.

51 Q. He, D. Tian, H. Jiang, D. Cao, S. Wei, D. Liu, P. Song, Y. Lin and L. Song, Achieving Efficient Alkaline Hydrogen Evolution Reaction over a Ni5P4 Catalyst Incorporating Single-Atomic Ru Sites, *Adv. Mater.*, 2020, **32**(11), 1906972, DOI: **10.1002/adma.201906972**.

52 D. Jin, H. Yoo, Y. Lee, C. Lee and M. H. Kim, IrO2–ZnO Composite Nanorod Array as an Acid-Stable Electrocatalyst with Superior Activity for the Oxygen Evolution Reaction, *ACS Appl. Energy Mater.*, 2022, **5**(3), 3810–3820, DOI: **10.1021/acsaem.2c00292**.

53 C. P. De Pauli and S. Trasatti, Composite Materials for Electrocatalysis of O2 Evolution: IrO2+SnO2 in Acid Solution, *J. Electroanal. Chem.*, 2002, **538–539**, 145–151, DOI: **10.1016/S0022-0728(02)01055-0**.

54 Y. Lai, Y. Li, L. Jiang, W. Xu, X. Lv, J. Li and Y. Liu, Electrochemical Behaviors of Co-Deposited Pb/Pb–MnO2 Composite Anode in Sulfuric Acid Solution – Tafel and EIS Investigations, *J. Electroanal. Chem.*, 2012, **671**, 16–23, DOI: **10.1016/j.jelechem.2012.02.011**.

55 J. G. Vos, T. A. Wezendonk, A. W. Jeremiasse and M. T. M. Koper, MnOx/IrOx as Selective Oxygen Evolution Electrocatalyst in Acidic Chloride Solution, *J. Am. Chem. Soc.*, 2018, **140**(32), 10270–10281, DOI: **10.1021/jacs.8b05382**.

56 B. E. Conway, G. Ping, A. De Battisti, A. Barbieri and G. Battaglin, Behaviour of the Adsorbed Cl˙ Intermediate in Anodic Cl2 Evolution at Thin-Film RuO2 Surfaces, *J. Mater. Chem.*, 1991, **1**(5), 725–734, DOI: **10.1039/JM9910100725**.

57 L. M. Da Silva, L. A. De Faria and J. F. C. Boodts, Electrochemical Ozone Production: Influence of the Supporting Electrolyte on Kinetics and Current Efficiency, *Electrochim. Acta*, 2003, **48**(6), 699–709, DOI: **10.1016/S0013-4686(02)00739-9**.

58 L. M. Da Silva, L. A. De Faria and J. F. C. Boodts, Green Processes for Environmental Application. Electrochemical Ozone Production, *Pure Appl. Chem.*, 2001, **73**(12), 1871–1884, DOI: **10.1351/pac200173121871**.

59 E. R. Kötz and S. Stucki, Ozone and Oxygen Evolution on PbO2 Electrodes in Acid Solution, *J. Electroanal. Chem. Interfacial Electrochem.*, 1987, **228**(1), 407–415, DOI: **10.1016/0022-0728(87)80120-1**.

60 C. C. L. McCrory, S. Jung, I. M. Ferrer, S. M. Chatman, J. C. Peters and T. F. Jaramillo, Benchmarking Hydrogen Evolving Reaction and Oxygen Evolving Reaction Electrocatalysts for Solar Water Splitting Devices, *J. Am. Chem. Soc.*, 2015, **137**(13), 4347–4357, DOI: **10.1021/ja510442p**.

